PERGAMON

International Journal of Heat and Mass Transfer 45 (2002) 1823–1838

International Journal of HEAT and MASS TRANSFER

www.elsevier.com/locate/ijhmt

Flow and heat transfer in rotating two-pass rectangular channels (AR = 2) by Reynolds stress turbulence model

Mohammad Al-Qahtani [a], Yong-Jun Jang [a], Hamn-Ching Chen [b,*], Je-Chin Han [c]

[a] *Turbine Heat Transfer Laboratory, Department of Mechanical Engineering, Texas A&M University, College Station, TX 77843, USA*
[b] *Ocean Engineering Program, Department of Civil Engineering, Texas A&M University, College Station, TX 77843, USA*
[c] *Turbine Heat Transfer Laboratory, Department of Mechanical Engineering, Texas A&M University, College Station, TX 77843, USA*

Received 26 March 2001; received in revised form 1 September 2001

Abstract

Numerical predictions of three-dimensional turbulent flow and heat transfer are presented for a rotating two-pass smooth rectangular channel with channel aspect ratio of 2:1. The focus of this study is to investigate the effect of rotation, channel orientation and the sharp 180° turn on the flow and heat transfer distributions. Two channel orientations are studied: $\beta = 90°$ and $\beta = 135°$. A multi-block Reynolds-averaged Navier–Stokes (RANS) method was employed in conjunction with a near-wall second-moment turbulence closure. The Reynolds number (Re) is fixed at 10,000 while the rotation number (Ro) is varied from 0 to 0.22. Two inlet coolant-to-wall density ratios $\Delta\rho/\rho$ are studied (0.115 and 0.22). The numerical results are compared with the experimental data for both stationary and rotating two-pass rectangular channels.

1. Introduction

As turbine inlet temperature increases in the gas turbine engine so does the heat load to the turbine blades. Therefore, highly sophisticated cooling technologies such as film cooling, impingement cooling and augmented convection cooling must be employed to maintain an acceptable blade life. This computational study considers the characteristics of the flow and local heat transfer in turbine coolant passages, which are important in predicting blade temperature and life. As a result of rotation and large coolant-to-wall temperature difference, the local heat transfer coefficients in turbine blade internal coolant passages are significantly different from those of stationary channels. For the coolant passage with radial outflow, the Coriolis induced secondary flows transport cooler fluid from the core to the trailing surface and enhance the local heat transfer on that side. The centrifugal buoyancy forces, due to the temperature difference between the cooler fluid and warmer surfaces, accelerate the streamwise velocity near the trailing surface and slow it down near the leading surface for outward flow. For the coolant passages with a 180° sharp turn, the high pressure gradient in the turn affects considerably the secondary flow field and the heat transfer. This complex coupling of the Coriolis forces, centrifugal buoyancy forces and turn effects has challenged researchers to predict the flow and thermal behaviors in the rotating multi-pass cooling channels.

Some experimental and numerical studies have been conducted in this field. Our review is restricted to the turbulent flow and heat transfer studies in rotating coolant passages with smooth walls. Wagner et al. [1] performed experimental studies on rotating multi-pass square channels with smooth walls. They investigated the effect of Reynolds number, rotation number and a buoyancy parameter in the rotating coolant passages. Dutta and Han [2] investigated the local heat transfer coefficients in rotating smooth two-pass square channels with three channel orientations. They found that a change in the channel orientation about the rotating frame causes a change in the secondary flow structure and the associated flow and turbulence distribution. Consequently, the heat transfer coefficient from the

* Corresponding author. Tel.: +1-979-847-9468; fax: +1-979-862-8162.
E-mail address: hcchen@civilmail.tamu.edu (H.-C. Chen).

0017-9310/02/$ - see front matter
PII: S0017-9310(01)00292-7

Nomenclature

AR	channel aspect ratio
D_h, D	hydraulic diameter
H	heat transfer coefficient
K	thermal conductivity of coolant
Nu	local Nusselt number ($= hD/k$)
Nu_0	Nusselt number in fully-developed turbulent non-rotating tube flow ($= hD/k$)
Pr	Prandtl number
Re	Reynolds number ($= \rho W_b D_h/\mu$)
r_i	inner radius of turn
Ro	rotation number ($= \Omega D_h/W_b$)
R_r	radius from axis of rotation
S	streamwise distance
T	local coolant temperature
T_0	coolant temperature at inlet
T_w	wall temperature
W_b	bulk velocity in streamwise direction
β	angle of channel orientation measured from direction of rotation
ρ	density of coolant
$\Delta\rho/\rho$	inlet coolant-to-wall density ratio ($= (T_w - T_0)/T_w$)
Ω	rotational speed
θ	dimensionless temperature ($= (T - T_0)/(T_w - T_0)$)
μ	dynamic viscosity of coolant

individual surfaces changes. Soong et al. [3] conducted heat transfer experiments in rotating smooth one-pass duct with different aspect ratios ranging from 0.2 to 5.0. They concluded that the aspect ratio of the duct was a critical parameter in the secondary flow patterns. Azad et al. [4] studied the effect of the channel angle orientation ($\beta = 90°$ and $\beta = 135°$ from the direction of rotation) on two-pass rectangular channel. They found that the Nusselt number ratios for the first pass trailing and second pass leading surfaces with $\beta = 135°$ are lower than those with $\beta = 90°$. Whereas, the Nusselt number ratios in the first pass leading and second pass trailing with $\beta = 135°$ are higher compared to those with $\beta = 90°$.

In addition to the experimental studies mentioned above, several studies have been made to numerically predict the flow and heat transfer in radially rotating ducts and ducts with 180° bends. Iacovides and Launder [5] performed a parametric study of the fully developed constant-density turbulent flow and heat transfer in rotating one-pass square and rectangular ducts (AR = 2:1) with normal channel orientation from the direction of rotation, i.e., $\beta = 90°$. They used the standard high-*Re* number k–ε model in the duct core while one equation low-*Re* turbulence model was used in the near-wall region. The rotational buoyancy effects were not included in their study. They concluded that rotational effects are not as strong in the rectangular rotating duct as in the square duct. Prakash and zerkle [6] (one passage), Dutta et al. [7] (one passage) and Sathyamurthy et al. [8] (two passages) presented the numerical results for rotating square duct with smooth walls and $\beta = 90°$. Their results showed that a high-*Re* k–ε model with wall function treatment in the near-wall region could not provide accurately the flow and heat transfer predictions and more refined turbulence models (low-*Re* k–ε model, two-layer model or second-moment closure model) should be used to get better results for this complex flow. Bo et al. [9] studied developing turbulent flow and heat transfer in a rotating one pass square duct, $\beta = 90°$. They adopted three turbulence models: a k–ε eddy viscosity model (EVM) matched with a low-*Re* number one-equation (EVM) model in the near-wall region, a low-*Re* k–ε EVM and a low-*Re* algebraic stress model (ASM). The k–ε/one-equation model and low-*Re* ASM model produced reasonable flow and thermal behaviors. In contrast, low-*Re* k–ε predictions showed unrealistic results. They concluded that it is necessary to employ low-*Re* second moment closure model to capture the flow behavior satisfactorily.

Stephens et al. [10] predicted the three-dimensional flow in a rotating two passage square duct with smooth walls and $\beta = 90°$. They employed a low Reynolds number k–ω turbulence model. Their computed heat transfer coefficients in the first passage were compared reasonably well with Wagner et al. [1] data, except on the leading surface where the heat transfer coefficients were overestimated by this model. However, a complete comparison with data was rendered difficult due to the different bend shapes. Iacovides et al. [11,12] explored turbulence modeling issues related to duct flows influenced by strong curvature and rotation ($\beta = 90°$). They tested four turbulence models: a high-*Re* k–ε model with one equation in the near-wall regions, a high-*Re* algebraic second-moment (ASM) closure with one equation in the near-wall regions, a low-*Re* ASM model where the dissipation rate of turbulence is obtained algebraically within the wall sublayers, and a low-*Re* ASM model where the ε transport equation is solved over the entire flow domain. The computations of flow through a stationary 180° bend suggest that turbulence anisotropy within the duct core and the wall sublayers have a strong influence on the development of flows affected by strong curvature. They concluded that more refined turbulence models are necessary to improve the predictions (they did not consider the energy transport in the duct).

Bonhoff et al. [13] presented the heat transfer predictions for a rotating 180° bend coolant channels ($\beta = 90°$). The differential Reynolds stress model (RSM) with wall function in FLUENT code was used for the calculation. The averaged heat transfer predictions were close to Wagner et al. [1] experimental results in the first passage of the channel, while the heat transfer in the second passage was overestimated by the RSM.

Chen et al. [14,15] predicted the flow and heat transfer in a rotating smooth two-pass square channel which is the first two passages of the four-pass, serpentine passage that was experimentally investigated by Wagner et al. [1]. They used two turbulence models: a two-layer k–ε isotropic eddy viscosity model and a near-wall second-moment closure model. The near-wall second-moment closure model accurately predicted the complex three-dimensional flow and heat transfer characteristics resulting from the rotation and strong wall curvature. They provided the most reliable predictions in comparison with the data of Wagner et al. [1]. This affirmed the superiority of the second-moment closure model compared to simpler isotropic eddy viscosity turbulence models. This model solves each individual Reynolds stress component directly from their respective transport equation. The primary advantage of this model is that it resolves the near-wall flow all the way to the solid wall rather than using log-law assumption in the viscous sublayer. With this near-wall closure, surface data like heat transfer coefficients and friction coefficients can be evaluated directly from velocity and temperature gradients on the solid wall.

In practice, the aerodynamic shape of the turbine blade dictates the use of cooling channels that are rectangular in cross-section and are at an angle β from the direction of rotation. The effect of rotation, channel orientation and sharp 180° turn on the secondary flow and heat transfer in rectangular channels may vary from the square channels. None of the previous studies predicted the characteristics of fluid flow and heat transfer in rotating rectangular two-pass channels that are either perpendicular or at an angle from the direction of rotation. In the present study, the second-moment RANS method of Chen et al. [14,15] is used to predict the three-dimensional flow and heat transfer for the rotating smooth two-pass rectangular duct (AR = 2:1) with 180° sharp turn. Moreover, this study investigates the effects of the channel orientation ($\beta = 90°$ and 135°) on the flow and heat transfer for the same geometry. The Reynolds number (Re) was fixed at 10,000. To explore the effect of rotation and centrifugal buoyancy force on the heat transfer, the rotation number (Ro) was varied from 0 to 0.22 and two inlet coolant-to-wall density ratios ($\Delta\rho/\rho$) were examined (0.115 and 0.22). The numerical results are compared with the experimental data for both the stationary and rotating rectangular two-pass channels.

2. Description of problem

Calculations were performed for the two-pass rectangular channel with smooth walls as tested by Azad et al. [4]. Fig. 1(a) shows the geometry, the axial stations at which results are presented and the way to view them. The geometry consists of a U-shaped smooth channel of rectangular cross-section with channel aspect ratio of 2:1. The channel is made up of two straight passages and a 180° sharp turn. Two of the four side walls, in the rotational direction, are denoted as the leading and trailing surfaces, respectively, while the other two side walls are denoted as the inner and outer surfaces. The channel hydraulic diameter, D_h, is 2/3 in (1.69 cm). The distance between the inlet of the channel and the axis of rotation (Y-axis) is given by $R_r/D_h = 20.0$. The length of each of the first and second passages is given as $L/D_h = 20.34$. Each passage consists of an unheated and a heated sections. The length of the unheated section is given by $L_1/D_h = 12.84$. It extends from the channel inlet to $Z = L_1$ in the first passage and from the channel exit to $Z = L_1$ in the second passage. The arc length S is measured from the beginning of the heated section in the first passage to the end of the heated section in the second passage. The radius of curvature of the 180° sharp turn is given as $r_i/D_h = 0.375$. Two channel orientations are studied: $\beta = 90°$ corresponding to the mid-portion of a turbine blade and $\beta = 135°$ corresponding to the serpentine passages in the trailing edge region of a blade. In this study, the Reynolds number (Re) is fixed at 10,000. The rotation number (Ro) is varied from 0 to 0.22 and two inlet coolant-to-wall density ratios ($\Delta\rho/\rho$) are studied (0.115 and 0.22). A summary of the cases studied is given in Table 1.

3. Computational procedure

3.1. Overview

The Reynolds-averaged Navier–Stokes (RANS) equations in conjunction with a near-wall Reynolds stress turbulence model are solved using the chimera RANS method of Chen et al. [14,15]. The governing equations with the second-moment closure turbulence model were described in detail by Chen et al. [14,15] and will not be repeated here. The flow is considered to be incompressible since the Mach number is quite low. However, the density in the centrifugal force terms is approximated by $\rho = \rho_0 T_0/T$ to account for the density variations caused by the temperature differences, where ρ_0 and T_0 are the density and temperature at the inlet of the cooling channel. In general, the density is also a function of the rotating speed because the centrifugal force creates a pressure gradient along the duct. In the experiments of Azad et al. [4], the maximum pressure

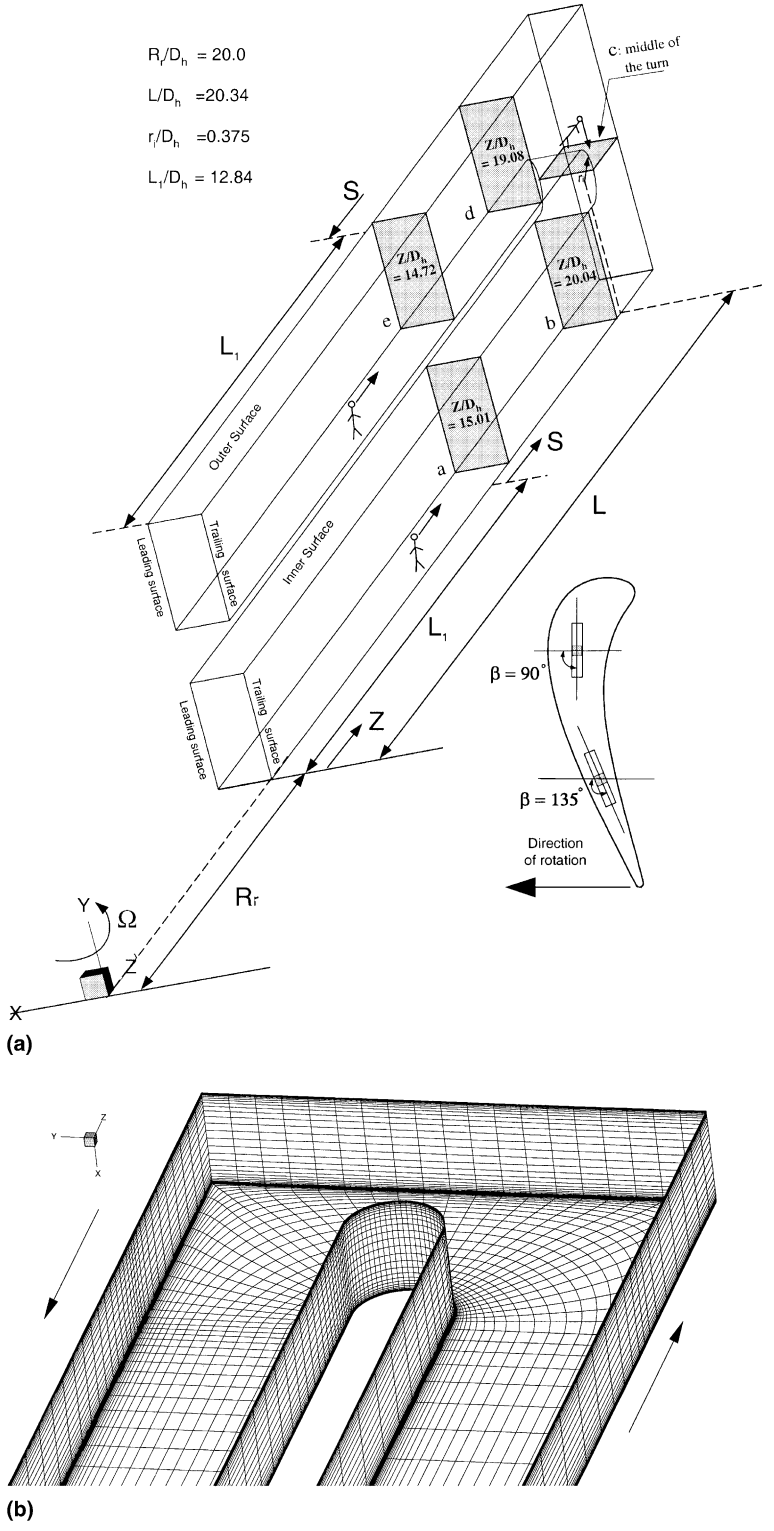

Fig. 1. (a) Geometry; (b) numerical grid.

Table 1
Summary of cases studied, $Re = 10,000$

Case #	Ro	$\Delta\rho/\rho$	β
1	0.00	0.115	–
2	0.11	0.115	90°
3	0.22	0.115	90°
4	0.22	0.220	90°
5	0.11	0.115	135°
6	0.22	0.115	135°
7	0.22	0.220	135°

variation between the channel inlet and the center of the bend is approximately 0.0067 atm for the highest rotation number of 0.22 (i.e., $\Omega = 550$ rpm) considered in the present study. This gives a maximum density variation of only about 0.67% from the inlet to the bend at the highest rotation number. It is therefore reasonable to omit the density variation caused by the pressure gradients induced by the channel rotation.

3.2. Chimera RANS method

The present method solves the mean flow and turbulence quantities in arbitrary combinations of embedded, overlapped, or matched grids using a chimera domain decomposition approach. In this approach, the solution domain was first decomposed into a number of smaller blocks to facilitate efficient adaptation of different block geometries, flow solvers, and boundary conditions for calculations involving complex configurations and flow conditions. Within each computational block, the finite-analytic numerical method of Chen et al. [16] was employed to solve the unsteady RANS equations on a general curvilinear, body-fitted coordinate system. The coupling between the pressure and velocity was accomplished using the hybrid PISO/SIMPLER algorithm of Chen and Korpus [17]. The method satisfied continuity of mass by requiring the contravariant velocities to have a vanishing divergence at each time step. Pressure was solved using the concept of pseudo-velocities and, when combined with the finite-analytic discretization gives the Poisson equation for pressure. To ensure the proper conservation of mass and momentum between the linking grid blocks, the grid–interface conservation techniques of Chen and Chen [18] were employed to eliminate the unphysical mass source resulting from the interpolation errors between the chimera grid blocks. In the present study, the numerical grids in the block overlap region are fully matched. Therefore, the grid–interface conservation is automatically satisfied.

3.3. Boundary conditions

A uniform velocity profile was used at the inlet of the duct ($Z = 0$) with all turbulence quantities set to zero. The unheated length (L_1) was long enough for the velocity profile to be fully developed turbulent profile before the heating start-point ($Z = L_1$). At the exit of the duct, zero-gradient outflow boundary conditions were employed for the mean velocity and all turbulent quantities, while linear extrapolation was used for the pressure field. The coolant fluid at the inlet of the duct is air at uniform temperature $T = T_0$ (i.e., $\theta = (T - T_0)/(T_w - T_0) = 0$). The wall temperature of the unheated section is kept constant at $T = T_0$ ($\theta = 0$) while the wall temperature of the heated section is kept constant at $T = T_w$ ($\theta = 1$). It should be noted that the present wall temperature boundary conditions are not exactly the same as the experimental conditions. In Azad et al. [4], the heat fluxes were maintained at constant rates on the leading, trailing, inner, and outer surfaces, but with different heat flux levels. The heat flux on each surface was adjusted independently to achieve nearly uniform temperature distributions in the circumferential direction. However, there are notable temperature variations along the channel caused by heat losses on each wall so the actual wall boundary conditions were neither constant heat flux nor constant temperature. These differences in the numerical and experimental wall boundary conditions must be borne in mind when comparing the predictions with the data.

3.4. Computational grid details

Fig. 1(b) shows the computational grid around the sharp 180° turn. The grid was elliptically generated using an interactive grid generation code GRIDGEN [19]. To provide adequate resolutions of the viscous sublayer and buffer layer adjacent to a solid surface, the minimum grid spacing in the near-wall region is maintained at 10^{-3} of the hydraulic diameter which corresponds to a wall coordinate y^+ of the order of 0.5. Extensive grid refinement studies were performed in Chen et al. [14,15] for two-pass smooth channel of a square cross-section. In those two studies, it was shown that a grid of $41 \times 41 \times 111$ was nearly grid independent. Also, it was found that the grid refinement in the streamwise direction has minor effects on the Nusselt number distribution. Since the present geometry is similar to the smooth square duct investigated in the aforementioned studies (except for the cross-section), 125 grid points were used in the streamwise direction. For the cross-section grid distribution, a separate grid refinement study was performed to examine the effect of the grid distribution in the cross-stream directions. Two grid distributions were used with the implementation of a general chimera domain decomposition technique [20,21]. Grid 1 has 33×41 grid in the cross-stream directions while Grid 2 was refined to 51×61. The Nusselt number was improved by 1% between the two grids. Therefore, Grid 1 ($33 \times 41 \times 125$) is considered to be nearly grid

independent and it was used in all of the results in the following discussions. In all calculations, the root-mean-square (rms) and maximum absolute errors for both the mean flow and turbulence quantities were monitored for each computational block to ensure complete convergence of the numerical solutions and a convergence criterion of 10^{-5} was used for the maximum rms error.

4. Results and discussion

As summarized in Table 1, computations were performed for one Reynolds number (10,000), three rotation numbers (0, 0.11 and 0.22) and two inlet coolant-to-wall density ratios $\Delta\rho/\rho$ (0.115 and 0.22) with two channel orientations of $\beta = 90°$ and 135°. The Nusselt numbers presented here were normalized with a smooth tube correlation by Dittus–Boelter/McAdams [22] for fully developed turbulent non-rotating tube flow

$$Nu_0 = 0.023\,Re^{0.8}\,Pr^{0.4}.$$

4.1. Velocity and temperature fields

Before discussing the detailed computed velocity field, a general conceptual view about the secondary flow patterns induced by Reynolds stress anisotropy, sharp turn, rotation and combined effect of rotation and sharp turn are summarized and sketched in Fig. 2. Also, locations of possible flow reversal are indicated in the figure. For the non-rotating case, Fig. 2(a) shows a magnified view of the Reynolds-stress-anisotropy induced vortices in the first passage and the turn-only induced vortices that continue to prevail in the second passage. Fig. 2(b) and (c) show the rotation-only induced vortices in the first and second passages and the combined effect of the rotation and turn induced vortices in the second passage. Also, it should be noted that in the 135° case, we define the corner of the leading and inner surfaces in the first passage as the first passage leading corner. Similarly, we define the corner of the first passage trailing and outer surfaces as the first passage trailing corner. Similar argument is used for the second passage.

At several axial stations as defined in Figs. 1(a) and 3–5 show the calculated secondary flow vectors and constant temperature contours for three cases out of the seven cases mentioned in Table 1. These cases are the non-rotating case (no. 1), the high rotating case of $\beta = 90°$ (no. 4: $Ro = 0.22$ and $\Delta\rho/\rho = 0.22$) and the high rotating case of $\beta = 135°$ (no. 7: $Ro = 0.22$ and $\Delta\rho/\rho = 0.22$). Note that stations a and b (the first passage) are viewed from upstream of the first passage, while stations c–e (middle of the turn and the second passage) are viewed from downstream of the second passage as shown in Fig. 1(a).

It can be seen from Fig. 3(a) that small secondary corner vortices are generated as a result of the Reynolds stress anisotropy in the first passage. The magnitude of these vortices, which is very small, cannot be seen clearly in this figure but they can be visualized through the conceptual view in Fig. 2(a) (first passage). It can be

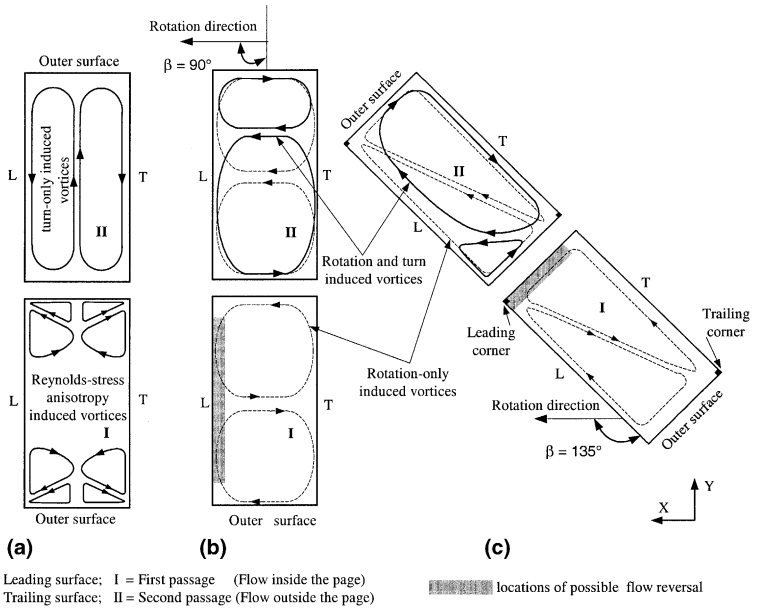

Fig. 2. Conceptual view of the secondary flow induced by sharp turn, rotation and combined effect of sharp turn and rotation. (a) Non-rotating case; (b) rotating case, $\beta = 90°$; (c) rotating case, $\beta = 135°$.

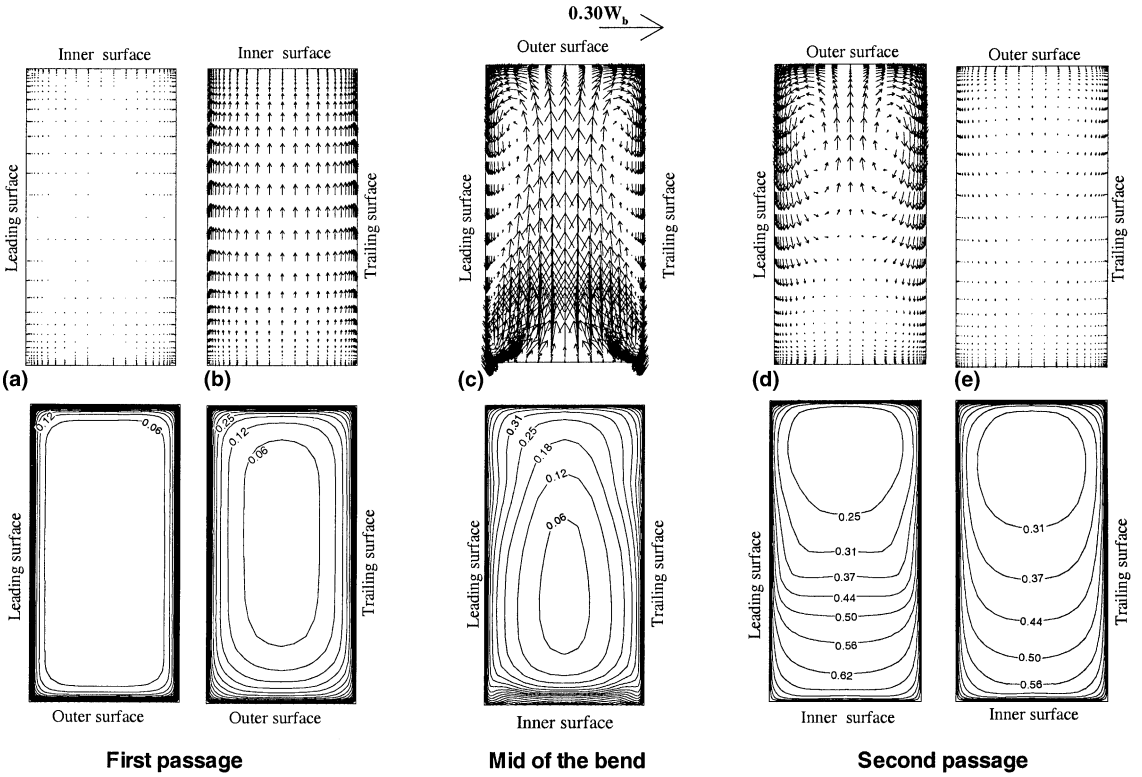

Fig. 3. Secondary flows and dimensionless temperature ($\theta = (T - T_0)/(T_w - T_0)$) for non-rotating duct, $Ro = 0.0$ and $\Delta\rho/\rho = 0.115$. (a) $Z/D = 15.01$; (b) $Z/D = 20.04$; (c) mid of the bend; (d) $Z/D = 19.08$; (e) $Z/D = 14.72$.

noticed from the corresponding temperature contour plots that the cooler fluid in the first passage is located in the core region of the channel cross-section. Just before the turn (Fig. 3(b)), the low pressure near the inner surface and high pressure near the outer surface induce a secondary flow that moves from the outer to the inner surface. Further through the sharp turn, two symmetric counter-rotating vortices develop gradually and reach their full size by the center of the turn (Fig. 3(c)). These two counter-rotating vortices are induced by the pressure gradient between the inner and outer surface. They convect fluid from the core towards the outer surface, resulting in a steeper temperature gradient and thus a higher heat transfer coefficient on the outer surface. At the beginning of the second passage, these two vortices remain to exist but detach from the inner surface (Fig. 3(d)) and their centers shift toward the outer wall. This detachment is due to a large separation bubble that occurs immediately downstream of the turn near the inner surface (see also Fig. 6(a)). These turn induced vortices remain to exist for about five hydraulic diameters from the beginning of the second passage (Fig. 3(d)). They disappear gradually as we move further downstream of the second passage (Fig. 3(e)). Note that the cooler fluid in this region of the second passage exists near the outer surface.

In Fig. 4, the Coriolis forces in the first passage produce a cross-stream two vortex flow structure (Fig. 4(a)) that pushes the cold fluid from the core toward the trailing surface and then brings it back along the inner and outer surfaces to the leading surface. This means that the thermal boundary layer starts at the trailing surface, grows along the two side surfaces and ends at the leading surface. This results in small temperature gradient near the leading surface (hence lower heat transfer coefficients) and steeper one near the trailing surface (hence higher heat transfer coefficients) as seen from the corresponding contour plot of Fig. 4(a). Moreover, the cooler heavier fluid near the trailing surface will be accelerated by the centrifugal buoyancy force while the hotter lighter fluid near the leading surface will be decelerated to maintain the continuity in the streamwise direction. Hence, if there is a flow reversal in the streamwise direction, it should take place on the leading surface (see Fig. 2(b)). As it will be shown later (Fig. 7(b)), flow reversal occurs in case 4 but not in cases 2 or 3. Before the sharp turn (Fig. 4(b)), the Coriolis induced secondary flow is distorted slightly by the

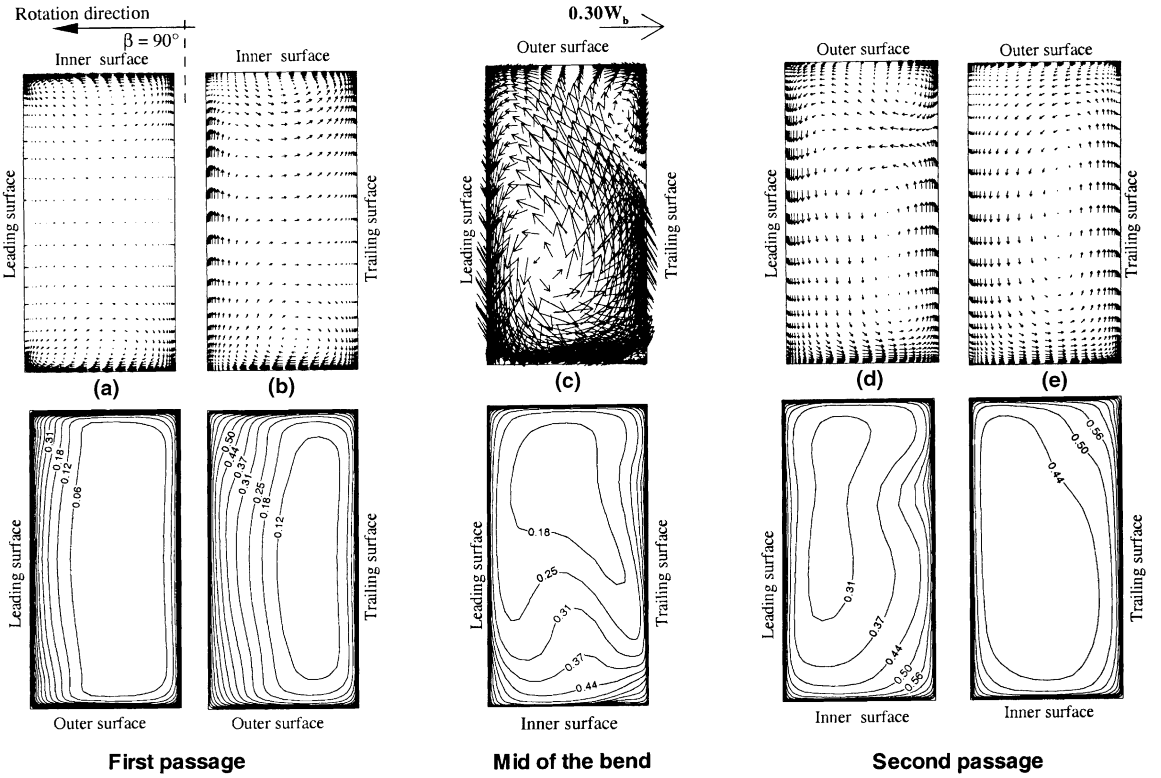

Fig. 4. Secondary flows and dimensionless temperature ($\theta = (T - T_0)/(T_w - T_0)$) for $Ro = 0.22$, $\Delta\rho/\rho = 0.22$ and $\beta = 90°$. (a) $Z/D = 15.01$; (b) $Z/D = 20.04$; (c) mid of the bend; (d) $Z/D = 19.08$; (e) $Z/D = 14.72$.

pressure gradient effect. In the middle of the turn (Fig. 4(c)), the two symmetric counter-rotating vortices induced by the tightly wound 180° sharp turn (in the stationary case) were found to be strongly disrupted by rotation. This results into a considerable growth of the vortex near the leading surface at the expense of the one next to the trailing surface, which becomes weaker and moves toward the outer surface. This results in pushing the cold fluid toward the outer surfaces as seen in the corresponding contour plot. This turn induced secondary flows combine with the rotation induced secondary flow in the second passage (Fig. 4(d) and (e)) and persist for a considerable distance downstream of the turn resulting in the pattern shown schematically in Fig. 2(b).

The Coriolis forces, in the first passage (Fig. 5(a)), produce a secondary flow that pushes the cold fluid diagonally away from the leading corner toward the trailing corner at which part of the secondary flow will move along the trailing-inner surface while the other part move along the outer-leading surface such that they meet again at the leading corner. This means that the thermal boundary layer starts at the trailing corner, grows along the trailing-inner surface and the outer-leading surface and ends at the leading corner. As a consequence of this, the fluid adjacent to outer surface (especially near the trailing corner) will be cold and heavy while the fluid adjacent to inner surface (especially near the leading corner) will be hot and light. Thus, the cooler heavier fluid near the trailing corner will be accelerated by the centrifugal buoyancy force while the hotter lighter fluid near the leading corner will be decelerated to maintain the continuity in the streamwise direction. Thus, if there is a flow reversal, it should take place on the inner surface for this 135° case and not on the leading surface as found in the 90° case (see also Fig. 2(c)). As it will be shown later (Fig. 6(c)), flow reversal occurs in case 7 but not in cases 5 or 6. Another consequence is that the temperature gradient will be small in the vicinity of the leading corner (hence lower heat transfer coefficients) and steep in the vicinity of the trailing corner (hence higher heat transfer coefficients) as seen from the corresponding contour plot. Just before the turn (Fig. 5(b)), the pressure gradient induced secondary flow (whose direction is from the outer to the inner surfaces) distorts the Coriolis induced secondary flow. Compared to the 90° case (Fig. 4(c)), the secondary flow field setup by rotation in the middle plane of the turn is not affected much by the change of the channel orientation (Fig. 5(c)) however the temperature contours change compared to the rotating 90° case. The turn in-

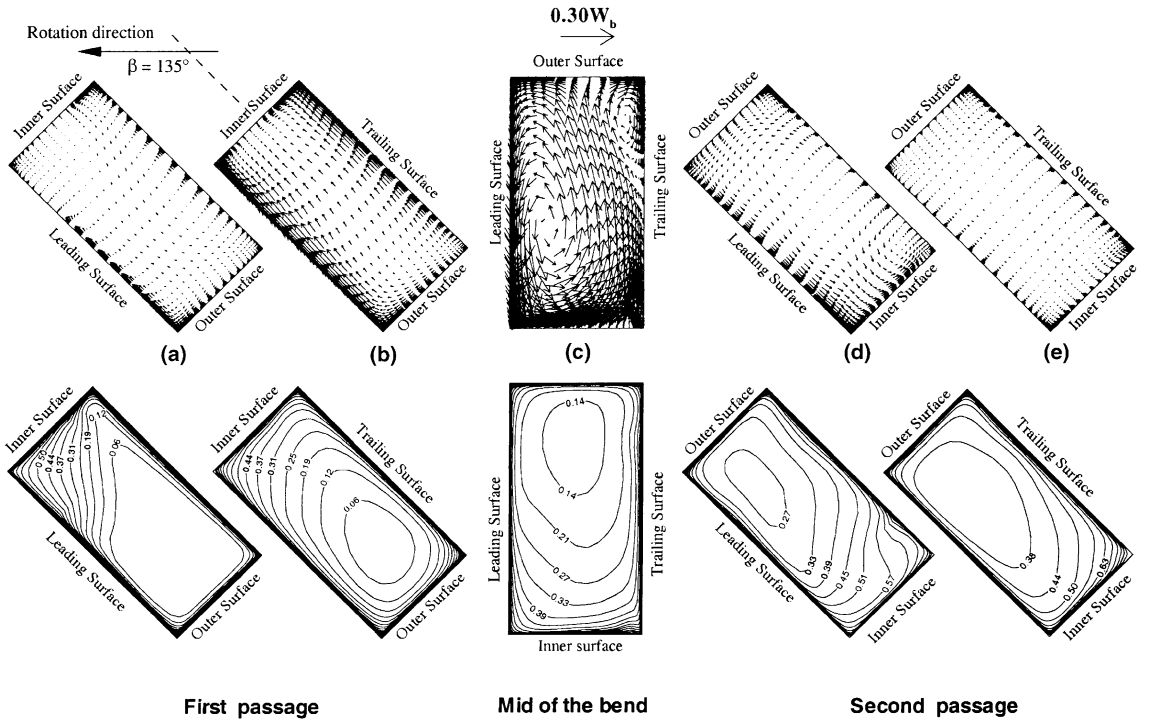

Fig. 5. Secondary flows and dimensionless temperature ($\theta = (T - T_0)/(T_w - T_0)$) for $Ro = 0.22$, $\Delta\rho/\rho = 0.22$ and $\beta = 135°$. (a) $Z/D = 15.01$; (b) $Z/D = 20.04$; (c) mid of the bend; (d) $Z/D = 19.08$; (e) $Z/D = 14.72$.

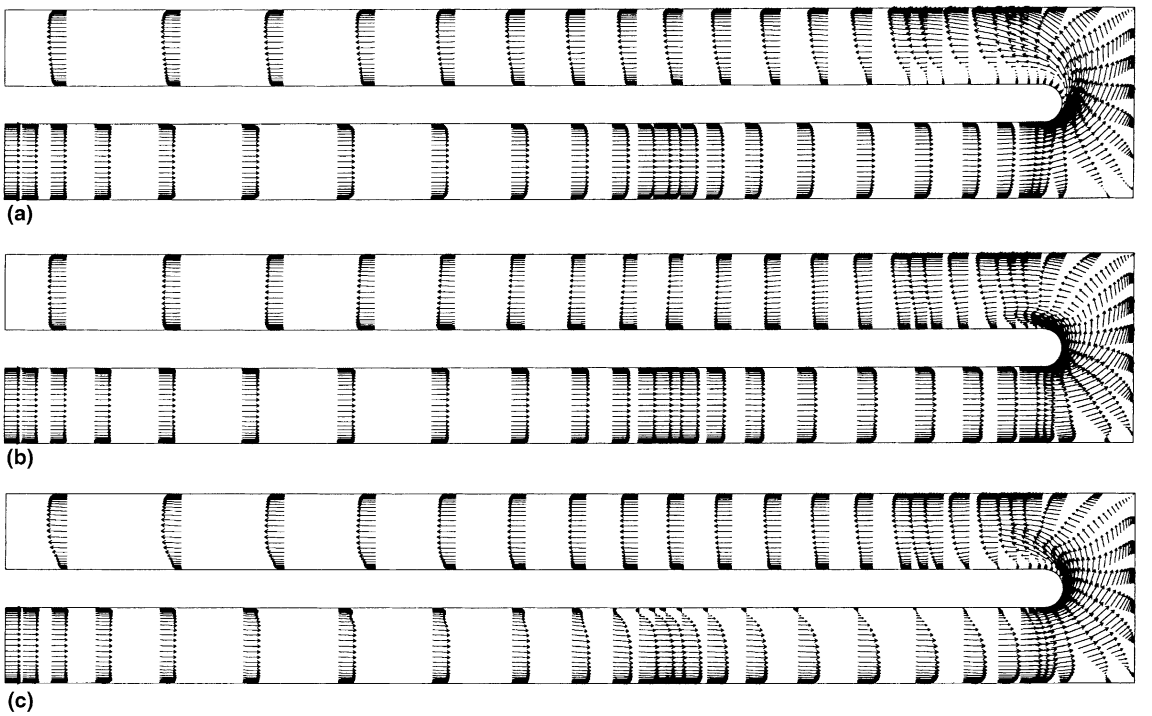

Fig. 6. Velocity vectors midway between leading and trailing surfaces. (a) $Ro = 0.0$, $\Delta\rho/\rho = 0.115$; (b) $Ro = 0.22$, $\Delta\rho/\rho = 0.22$, $\beta = 90°$; (c) $Ro = 0.22$, $\Delta\rho/\rho = 0.22$, $\beta = 135°$.

duced vortices combine with the rotation induced ones resulting in a complex secondary flow (Fig. 5(d) and (e)) which persists a considerable distance downstream of the turn resulting finally in the pattern shown schematically in Fig. 2(c). It should be mentioned that this combined pattern of the turn and rotation induced vortices (solid line in Fig. 2(c)) appears at different axial stations for different rotation numbers and density ratios. Case 7 takes the longest distance downstream of the turn for the above pattern to appear.

The velocity vector distribution in the planes midway between the leading and trailing surfaces are shown in Fig. 6. For the non-rotating case (Fig. 6(a)), the velocity profiles were flat before the turn. Upon entering the turn, the flow accelerates in the region near the inner wall and decelerates in the region near the outer wall. This behavior is caused by the favorable and adverse pressure gradients along the inner and outer surfaces, respectively. This pressure distribution is reversed at the beginning of the second passage and thus, the flow accelerates near the outer surface and decelerates near the inner surface. Due to the inability of the flow to follow the sharp turn, a fairly large separation bubble occurs downstream of the divider wall tip followed by a reattachment region that occurs about $3.0D_h$ from the beginning of the second passage. As the flow proceeds downstream of the second passage, the influence of the sharp 180° sharp turn gradually diminishes and the streamwise mean velocities, both near the outer and inner surfaces, gradually redevelop. For the 90° rotating case, Fig. 6(b) shows that the separation bubble disappears for rotation number $Ro = 0.22$. This is because the pressure rise in the radial direction due to the centrifugal force is reducing the adverse pressure gradient induced by the turn. As the flow proceeds downstream the second passage, the influence of the sharp 180° sharp turn quickly diminishes and the streamwise mean velocities, both near the outer and inner surfaces, redevelop faster compared to the stationary case. For the 135° rotating case, two results can be drawn from Fig. 6(c). First, flow reversal occurs in the first passage near the inner surface. It extends a considerable distance upstream of the turn entrance. As explained in the discussion of Fig. 5(a), this is a consequence of the cross-stream secondary flow and the centrifugal buoyancy force which accelerates the cooler fluid in the nearby region of the trailing corner while decelerates the hotter fluid in the nearby region of the leading corner (see also Fig. 2(c)). The second result is that a mild separation bubble occurs downstream of the divider wall tip followed by a reattachment region that occurs about $1.5D_h$ from the beginning of the second passage. The reason for that is that the pressure rise in the radial direction (due to the centrifugal force) in this 135° case did not overcome the adverse pressure gradient induced by the turn as was the case for the 90° case.

Figs. 7 and 8 show the velocity vector distribution and temperature contours in a plane midway between

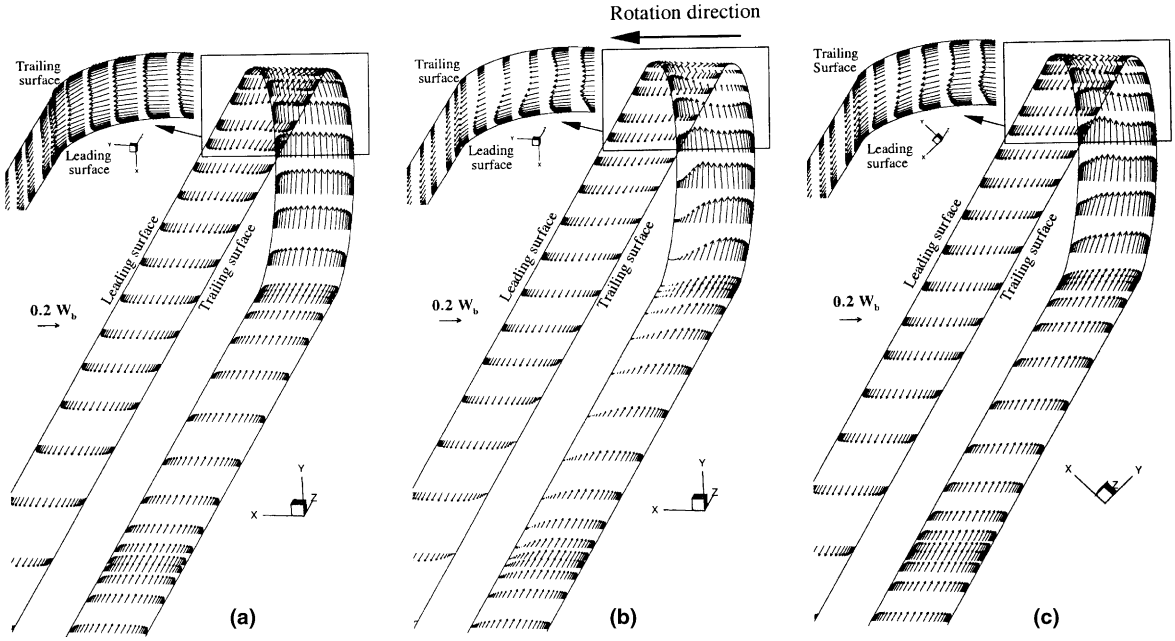

Fig. 7. Streamwise velocity vectors midway between inner and outer surfaces. (a) $Ro = 0.0$, $\Delta\rho/\rho = 0.115$; (b) $Ro = 0.22$, $\beta = 90°$, $\Delta\rho/\rho = 0.22$; (c) $Ro = 0.22$, $\beta = 135°$, $\Delta\rho/\rho = 0.22$.

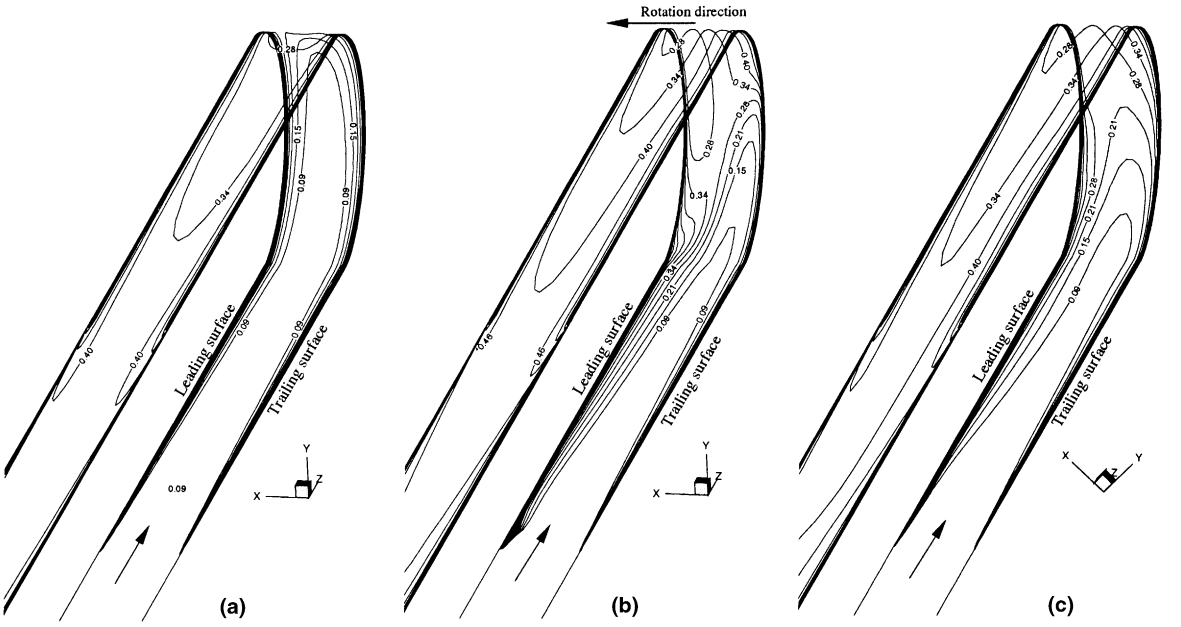

Fig. 8. Temperature contours midway between inner and outer surfaces. (a) $Ro = 0.0$, $\Delta\rho/\rho = 0.115$; (b) $Ro = 0.22$, $\beta = 90°$, $\Delta\rho/\rho = 0.22$; (c) $Ro = 0.22$, $\beta = 135°$, $\Delta\rho/\rho = 0.22$.

the inner and outer surfaces. To facilitate viewing the streamwise velocity profile development in the second corner of the turn (Fig. 7), this region is enlarged and rotated 90° around the Z-axis. The streamwise velocity profile remain flat and symmetric along the duct in the non-rotating case (Fig. 7(a)) and thus the cold fluid will remain in the middle between the leading and trailing surfaces in the streamwise direction as seen from the contour plot of Fig. 8(a). For the 90° rotating case, the following results are recorded:

1. The streamwise velocity profile is shifted toward the first passage trailing surface as a result of the Coriolis force (Fig. 7(b)). Therefore the cold fluid will exist near the trailing surface while the hot fluid will exist near the leading surface (Fig. 8(b)).
2. Flow reversal occurs near the first passage leading surface and extends to $8D_h$ upstream of the turn entrance. This is because the cold fluid near the trailing surface is accelerated in the outward direction by the centrifugal buoyancy force and hence the light fluid near the leading surface will be decelerated to maintain the flow continuity (see also Fig. 2(b)).
3. The streamwise velocity profile in the turn gradually shifts toward the leading surface (and so does the cold fluid) as a result of the change in the Coriolis force direction (Figs. 7(b) and 8(b): turn region).
4. In the second passage, the streamwise velocity profile is flattened (Fig. 7(b): second passage). This is because the Coriolis force pushes the cold fluid toward the leading surface (Fig. 8(b): second pass) resulting in its deceleration by the outward centrifugal buoyancy force and the acceleration of the lighter fluid near the trailing surface in the inward direction to maintain the flow continuity.

For the 135° rotating case, the streamwise velocity profile is slightly shifted toward the first passage trailing surface (Fig. 7(c)) and second passage leading surface because only part of the Coriolis force in the plane midway between the inner and outer surfaces act toward the first passage trailing surface and second passage leading surface. This can be more easily seen from the contour plots of Fig. 8(c) where less cold fluid is pushed toward the first passage trailing surface and second passage leading surface.

4.2. Detailed local heat transfer coefficient distribution

Fig. 9(a) shows the Nu/Nu_0 contour plots on the leading and trailing surfaces for the non-rotating case. The unheated sections in the first and second passages were cut to focus on the heated sections and turn effects. The Nusselt number ratios near the beginning of the heated first passage section are high due to the thinner boundary layers. Downstream, they decrease and asymptotically approach the fully developed value. Near the outer surface of the turn, the Nusselt number ratios are high due to the turn induced secondary flow. The Nusselt number ratios decrease downstream of the

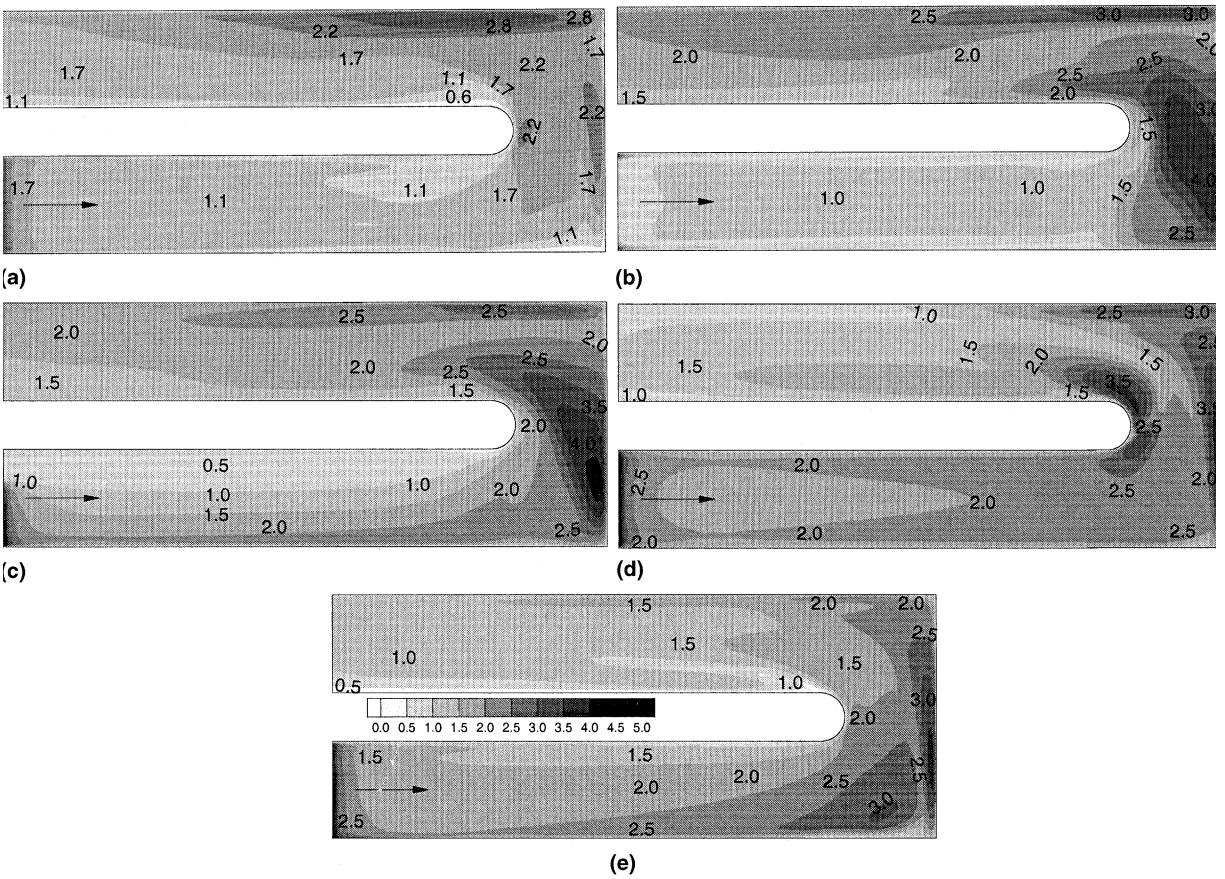

Fig. 9. Detailed Nusselt number distribution. (a) Leading and trailing surfaces ($Ro = 0.0$, $\Delta\rho/\rho = 0.115$); (b) leading surface ($Ro = 0.22$, $\Delta\rho/\rho = 0.22$, $\beta = 90°$); (c) leading surface ($Ro = 0.22$, $\Delta\rho/\rho = 0.22$, $\beta = 135°$); (d) trailing surface ($Ro = 0.22$, $\Delta\rho/\rho = 0.22$, $\beta = 90°$); (e) trailing surface ($Ro = 0.22$, $\Delta\rho/\rho = 0.22$, $\beta = 135°$).

second passage with the ones near the outer surface being higher than those near the inner surface due to the secondary flow effect in the second passage.

Fig. 9(b) shows the Nu/Nu_0 ratio contours on the leading side for the 90° high-rotation high-density-ratio case ($Ro = 0.22$ and $\Delta\rho/\rho = 0.22$). Compared to the non-rotating case, the heat transfer is lower in the first pass and higher in the second passage because of the Coriolis force induced secondary flow. The Nu/Nu_0 increases significantly next to the outer surface of the turn.

Fig. 9(c) shows the Nu/Nu_0 ratio contours on the leading side for the 135° high-rotation high-density-ratio case ($Ro = 0.22$ and $\Delta\rho/\rho = 0.22$). Along the first passage, the Nu/Nu_0 ratios are high next to the outer surface and then decrease toward the inner surface (leading corner). As explained in the velocity section, part of the cold fluid comes back from the trailing corner along the outer and leading surfaces. This means that the thermal boundary layer grows on the leading surface as the secondary flow moves to the leading corner and thus heat transfer decreases in this direction. The Nu/Nu_0 distribution in the turn and second passage is similar to the 90° rotating case.

Fig. 9(d) shows the Nu/Nu_0 ratio contours on the trailing side for the 90° high-rotation high-density-ratio case ($Ro = 0.22$ and $\Delta\rho/\rho = 0.22$). The heat transfer is higher in the first passage and lower in the second passage compared to the non-rotating case. This is again a result of the rotation induced secondary flow that pushes the cold fluid toward the first passage trailing surface and away from the second passage trailing surface (see the velocity section).

Fig. 9(e) shows the Nu/Nu_0 ratio contours on the trailing side for the 135° high-rotation high-density-ratio case ($Ro = 0.22$ and $\Delta\rho/\rho = 0.22$). Along the first passage, the Nu/Nu_0 is high next to the outer surface (trailing corner) and then decreases as we move to the inner surface for the same reason explained earlier. In the turn region, the Nusselt number still high but lower than the 90° rotating case.

4.3. Spanwise-averaged heat transfer coefficients and comparison with experimental data

Fig. 10 shows the effect of the rotation number and inlet coolant-to-wall density ratio on the Nusselt number ratio distributions for channel orientation of $\beta = 90°$. The rotation number is varied from 0 to 0.22 and two inlet coolant-to-wall density ratios ($\Delta\rho/\rho$) are used (0.115 and 0.22). The Reynolds number is fixed at 10,000. The Nusselt number ratios in the first passage trailing, inner and outer surfaces increase as the rotation number and density ratio increase. On the other hand, the Nusselt number ratios in the first passage leading surface initially decrease with an increase in the rotation number (cases 1–3) and later increases with higher density ratio (case no. 4). This behavior at the leading surface which was also noticed by Prakash and Zerkle [6] and Dutta et al. [7] is attributed to the adverse buoyancy driven flow separation that occurs next to the leading surface in the high-rotation high-density-ratio case (see Fig. 7(b)). Flow separation enhances turbulence and consequently heat transfer increases. The Nusselt number ratios in the beginning of the second passage leading and trailing surfaces are relatively unaffected by the variations in the rotation number and density ratio. With increasing distance downstream of the turn, the effect of the turn induced secondary flows decay and the rotational effects (Coriolis and buoyancy forces) on heat transfer become stronger though not as strong as in the first passage.

Fig. 11 shows the same information as Fig. 10 but for channel orientation of 135°. Next to the inlet, the Nusselt number ratios decrease with an increase in the rotation number and density ratio and then increase towards the turn. The Nusselt number ratios in the first passage trailing and outer surfaces increase with an increase in the rotation number and density ratio with the increase in the outer surface being the highest. This is expected because most of the outer surface will behave as a trailing surface. By the same reasoning, most of the inner surface will behave as a leading surface and hence we see that the Nusselt number ratios at the first passage inner surface decrease with an increase in the rotation number and density ratio.

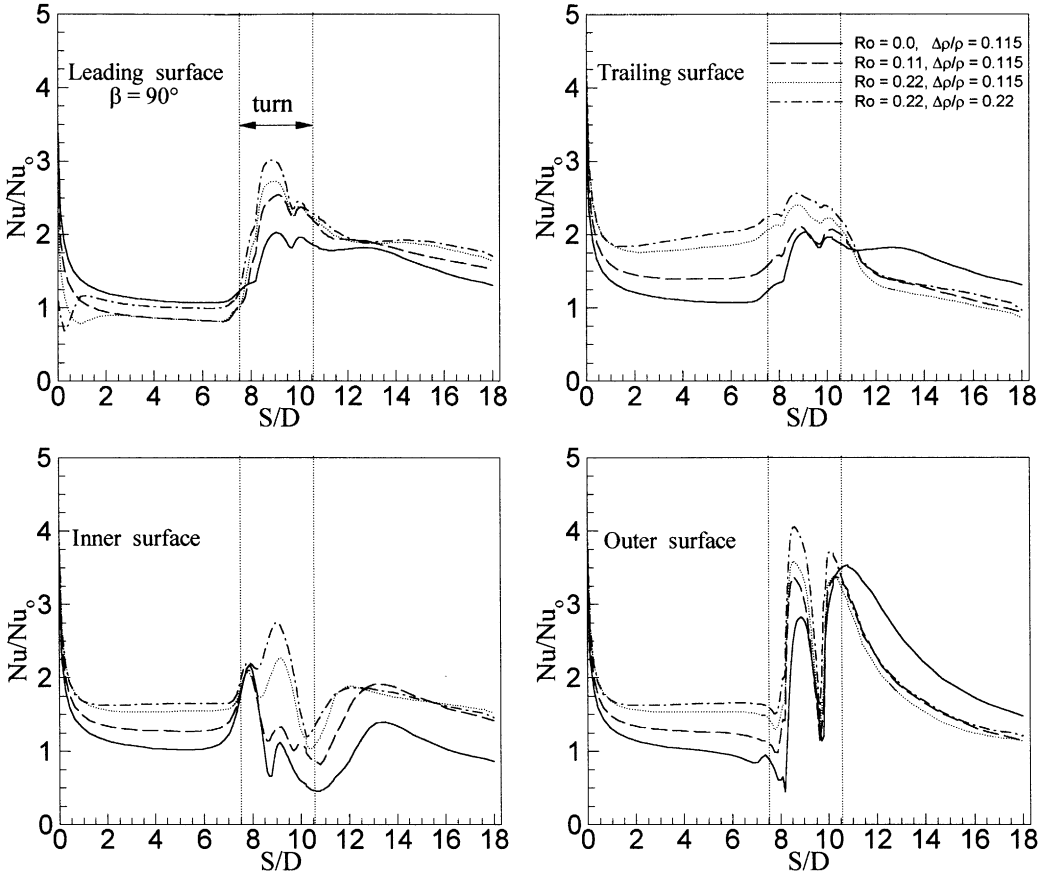

Fig. 10. Effect of the rotation number and coolant-to-wall density ratio on Nusselt number ratios, $Re = 10,000$ and $\beta = 90°$.

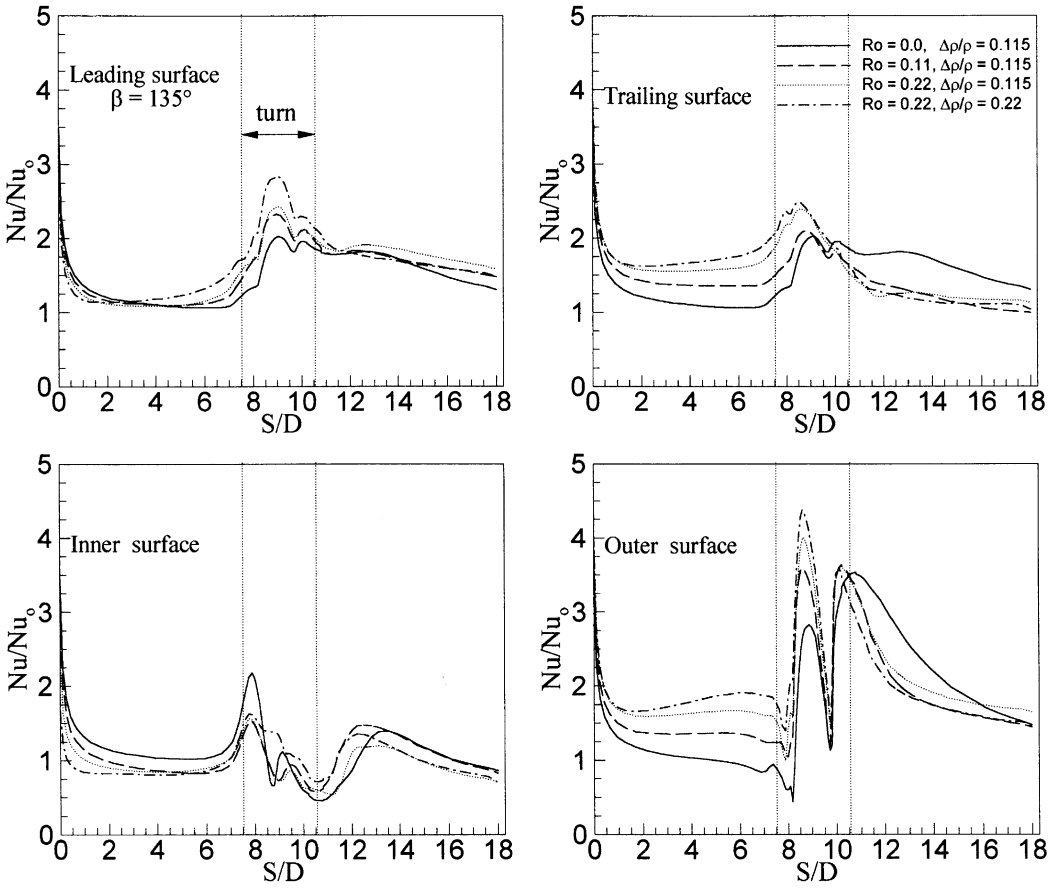

Fig. 11. Effect of the rotation number and coolant-to-wall density ratio on Nusselt number ratios, $Re = 10,000$ and $\beta = 135°$.

Comparisons of the spanwise-averaged Nusselt number ratios (Nu/Nu_0) were made with the experimental data of Azad et al. [4] in Fig. 12. In order to compare the effects of the channel orientation on the heat transfer, Fig. 12 shows the Nusselt number ratios for three cases: ($Ro = 0.0$, $Ro = 0.11$ ($\beta = 90°$), and $Ro = 0.11$ ($\beta = 135°$)). In this figure, the inlet coolant-to-wall density ratio was held constant at a value of 0.115. The effect of the model orientation can be seen by comparing the 135° Nusselt number ratios with the 90° ones. It can be seen that, in the first passage, the 135° Nusselt number ratios are: (a) higher on the leading surface and lower on the trailing surface, and (b) lower on the inner surface and higher on the outer surface. The reason behind that could be explained in the light of Fig. 2 where it can be seen that the cold fluid received by the 135° leading surface is cooler than that received by the 90° leading surface. This is because, in the 90° case, the cold fluid reaches the leading surface after it passes over half of the trailing surface and one of the two side surfaces. However, in the 135° case, the cold fluid moves directly to the trailing corner and passes only by the outer surface before it reaches the leading surface which means higher heat transfer compared to the 90° case. For the trailing surface, all of cold fluid (in the 90° case) moves along the trailing surface after it splits at its middle. On the other hand, the cold fluid in the 135° case moves first to the trailing corner at which only part of it will come back to the trailing surface which means less heat transfer compared to the 90° case. Downstream of the second passage, the Nusselt number ratios of the 90° and 135° rotating cases show similar heat transfer characteristics for both leading and trailing surfaces. The Nusselt number ratios in the turn are enhanced on all surfaces for all cases with the outer Nusselt number ratios being the highest. Comparisons with the experimental values reveal fair agreement on the leading and trailing sides except for the first three points on the trailing surface being underpredicted. This may be attributed to two reasons:

1. It is known that agreement with smooth surface data is hard because any surface imperfection on the copper plates will increase the heat transfer data compared to the computational results.

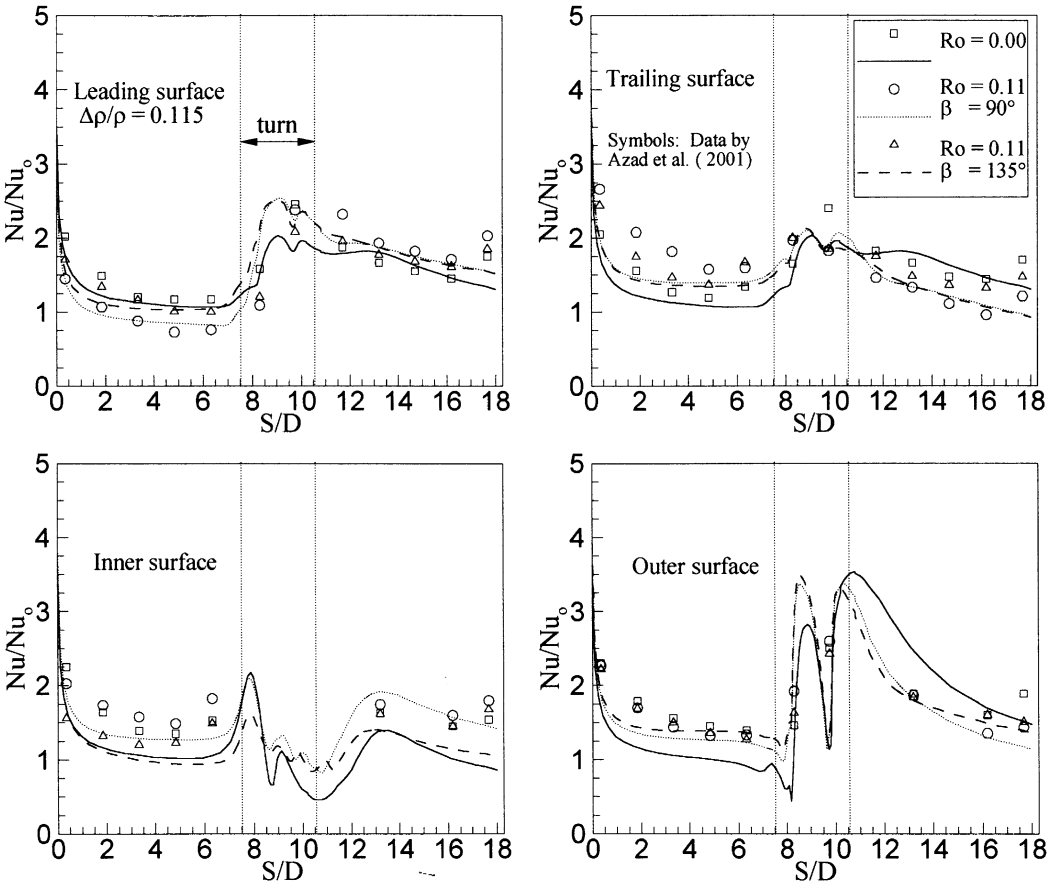

Fig. 12. Calculated and measured Nusselt number ratios, $Re = 10,000$.

2. The fact that the predicted Nusselt number ratios are based on a uniform wall temperature boundary condition while the experimental ones are based on a uniform wall heat flux boundary condition.

5. Conclusions

A multi-block RANS method was employed to predict three-dimensional flow and heat transfer in a rotating two-pass smooth rectangular channel with 180° sharp turn and aspect ratio of 2:1. Two channel orientations are studied: $\beta = 90°$ and 135°. The present near-wall second-moment closure model results were compared with the experimental data of Azad et al. [4]. It predicted fairly well the complex three-dimensional flow and heat transfer characteristics resulting from the sharp 180° turn, rotation, centrifugal buoyancy forces and channel orientation. The main findings of the study may be summarized as follows.

(a) *For the rotating 90° channel*:

- The Coriolis force induces secondary flow, in the first passage, which pushes the cold fluid from the leading to the trailing surface, and in the second passage, from the trailing to the leading surface, respectively.
- The buoyancy force, in the first passage, accelerates the cold fluid near the trailing surface and decelerates the hot fluid near the leading surface. This results in flow reversals on the first passage leading surface for the high-rotation high-density-ratio case ($Ro = 0.22$ and $\Delta\rho/\rho = 0.22$).
- The Nusselt number ratios on the first passage trailing and second passage leading surfaces increase with an increase in the rotation number and density ratio.

(b) *For the rotating 135° channel*:

- The Coriolis force induces secondary flow, in the first passage, which pushes the cold fluid from the leading to the trailing corner, and in the second passage, from the trailing to the leading corner, respectively.
- The buoyancy force, in the first passage, accelerates the cold fluid near the trailing corner and decelerates

the hot fluid near the leading corner. This results in flow reversals on the first passage inner surface for the high-rotation high-density-ratio case ($Ro = 0.22$ and $\Delta\rho/\rho = 0.22$).

- In the first passage, most of the inner surface behaves as a leading side and thus the Nusselt number ratios on the inner surface decrease with an increase in rotation number and density ratio which is opposite to the Nusselt number ratios trend on the 90° inner surface. Similarly, most of the outer surface and parts from the trailing surface behave as a trailing side. Thus, the increase in the Nusselt number ratios is higher on the outer surface when compared with their counterparts in the 90° rotating case.

Acknowledgements

The leading author, Mohammad Al-Qahtani, received a fellowship from King Fahd University; Saudi Arabia, for his Ph.D. study at Texas A&M University. This work was supported by the Texas Higher Education Coordination Board Advanced Technology Program under grant no. 999903-165. The computations were performed on the Cray J90 at the Texas A&M Supercomputer Center under a supercomputer research grant. Other computations were performed on the Cray C90 of Cray Research Inc. under the sponsorship of Frank Kampe. The GRIDGEN software was supported by Pointwise Inc. The support of all of the above institutions is greatly appreciated.

References

[1] J.H. Wagner, B.V. Johnson, F.C. Kopper, Heat transfer in rotating serpentine passage with smooth walls, J. Turbomachinery 113 (3) (1991) 321–330.
[2] S. Dutta, J.C. Han, Local heat transfer in rotating smooth and ribbed two-pass square channels with three channel orientations, J. Heat Transfer 118 (3) (1996) 578–584.
[3] C.Y. Soong, S.T. Lin, G.J. Hwang, An experimental study of convective heat transfer in radially rotating rectangular ducts, J. Heat Transfer 113 (1991) 604–611.
[4] G.M.S. Azad, M.J. Uddin, J.C. Han, H.K. Moon, B. Glezer, Rotating heat transfer in two-pass rectangular channels with 45° parallel and crossed rib turbulators, ASME International Gas Turbine and Aeroengine Congress, New Orleans, LA, June 4–7, 2001, Paper no. 2001-GT-186.
[5] H. Iacovides, B.E. Launder, Parametric and numerical study of fully developed flow and heat transfer in rotating rectangular ducts, J. Turbomachinery 113 (1991) 331–338.
[6] C. Prakash, R. Zerkle, Prediction of turbulent flow and heat transfer in a radially rotating square duct, J. Turbomachinery 114 (4) (1992) 835–846.
[7] S. Dutta, M.J. Andrews, J.C. Han, Prediction of turbulent heat transfer in rotating smooth square ducts, Int. J. Heat Mass Transfer 39 (12) (1996) 2505–2514.
[8] P.S. Sathyamurthy, K.C. Karki, S.V. Patankar, Prediction of turbulent flow and heat transfer in a rotating square duct with a 180 degree bend, ASME, 1994, Paper 94-GT-197.
[9] T. Bo, H. Iacovides, B.E. Launder, Developing buoyancy-modified turbulent flow in ducts rotating in orthogonal mode, J. Turbomachinery 117 (3) (1995) 474–484.
[10] M.A. Stephens, T.I.-P. Shih, K.C. Civinskas, Computations of flow and heat transfer in a rotating U-shaped square duct with smooth walls, AIAA, 1996, Paper no. 96-3161.
[11] H. Iacovides, D.C. Jackson, G. Kelemenis, B.E. Launder, Y.M. Yuan, Experiments on local heat transfer in a rotating square-ended U-bend, Int. J. Heat Fluid Flow 20 (3) (1999) 302–310.
[12] H. Iacovides, B.E. Launder, H.-Y. Li, The computation of flow development through stationary and rotating U-ducts of strong curvature, Int. J. Heat Fluid Flow 17 (1) (1996) 22–33.
[13] B. Bonhoff, U. Tomm, B.V. Johnson, I. Jennions, Heat transfer predictions for rotating U-shaped coolant channels with skewed ribs and with smooth walls, ASME, 1997, Paper 97-GT-162.
[14] H.C. Chen, Y.J. Jang, J.C. Han, Computation of heat transfer in rotating two-pass square channels by a second-moment closure model, Int. J. Heat Mass Transfer 43 (9) (2000) 1603–1616.
[15] H.C. Chen, Y.J. Jang, J.C. Han, Near-wall second-moment closure for rotating multi-pass cooling channels, J. Thermophys. Heat Transfer 14 (2) (2000) 201–209.
[16] H.C. Chen, V.C. Patel, S. Ju, Solutions of Reynolds-averaged Navier–Stokes equations for three-dimensional incompressible flows, J. Comput. Phys. 88 (2) (1990) 305–336.
[17] H.C. Chen, R. Korpus, A multi-block finite-analytic Reynolds-averaged Navier–Stokes method for 3D incompressible flows, in: ASME Fluids Engineering Conference, ASME FED-vol. 150, Washington, DC, June 20–24, 1993, pp. 113–121.
[18] H.C. Chen, M. Chen, Chimera RANS simulation of a berthing DDG-51 ship in translational and rotational motions, Int. J. Offshore Polar Eng. 8 (3) (1998) 82–191.
[19] GRIDGEN Users' Manual, Version 13.3, Pointwise Inc., 1999.
[20] B.J. Hubbard, H.C. Chen, A chimera scheme for incompressible viscous flows with applications to submarine hydrodynamics, 25th AIAA Fluid Dynamics Conference, Colorado Springs, CO, AIAA, 1994, Paper no. 94-2210.
[21] H.C. Chen, T. Liu, E.T. Huang, D.A. Davis, Chimera RANS simulation of ship and fender coupling for berthing operations, Int. J. Offshore Polar Eng. 10 (2) (2000) 12–122.
[22] W.M. Rohsenow, H. Choi, in: Heat, Mass and Momentum Transfer, Prentice-Hall, Englewood Cliffs, NJ, 1961, pp. 192–193.